Monthly Notices
of the
ROYAL ASTRONOMICAL SOCIETY

MNRAS **483,** 2836–2850 (2019)
Advance Access publication 2018 December 7

doi:10.1093/mnras/sty3327

Evidence for a clumpy disc-wind in the star-forming Seyfert 2 galaxy MCG–03–58–007

G. A. Matzeu [1,2★] V. Braito [2,3★] J. N. Reeves,[3] P. Severgnini,[4] L. Ballo [1] A. Caccianiga [4] S. Campana,[4] C. Cicone,[4] R. Della Ceca,[4] M. L. Parker [1] M. Santos-Lleó[1] and N. Schartel[1]

[1]*European Space Agency (ESA), European Space Astronomy Centre (ESAC), E-28691 Villanueva de la Cañada, Madrid, Spain*
[2]*INAF – Osservatorio Astronomico di Brera, Via Bianchi 46, I-23807 Merate (LC), Italy*
[3]*Center for Space Science and Technology, University of Maryland Baltimore County, 1000 Hilltop Circle, Baltimore, MD 21250, USA*
[4]*INAF – Osservatorio Astronomico di Brera, Via Brera 28, I-20121 Milano, Italy*

Accepted 2018 December 3. Received 2018 November 28; in original form 2018 August 1

ABSTRACT

We report the results of a detailed analysis of a deep simultaneous 130 ks *XMM–Newton* and *NuSTAR* observation of the nearby ($z = 0.0315$) and bright ($L_{\rm bol} \sim 3 \times 10^{45}$ erg s^{-1}) starburst–active galactic nucleus (AGN) Seyfert 2 system: MCG–03–58–007. From the broad-band fitting we show that most of the obscuration needs to be modelled with a toroidal type reprocessor such as `MYTorus`. None the less the signature of a powerful disc-wind is still apparent at higher energies and the observed rapid short-term X-ray spectral variability is more likely caused by a variable zone of highly ionized fast wind rather than by a neutral clumpy medium. We also detect X-ray emission from larger scale gas as seen from the presence of several soft narrow emission lines in the RGS, originating from a contribution of a weak star-forming activity together with a dominant photoionized component from the AGNs.

Key words: black hole physics – galaxies: active – galaxies: nuclei – quasars: individual: MCG–03–58–007 – X-rays: galaxies.

1 INTRODUCTION

It is widely accepted that the central engine of active galactic nuclei (AGNs) is powered by accretion of matter on to a supermassive black hole (SMBH). They are also thought to harbour circumnuclear material in a toroidal structure (i.e. dusty torus) that absorbs and reprocesses the high-energy radiation emitted from these central regions. Although the dusty torus is predicted to be ubiquitous in AGNs by the unification scheme (Antonucci 1993), the exact geometry, location and composition are poorly understood. None the less, important advances have been made in recent years through the observed long-term variability (i.e. months–years) of the X-ray absorber's column density ($N_{\rm H}$). This ruled out the standard view of a homogeneous 'doughnut' shaped absorber in favour of a more 'clumpy' torus (e.g. Risaliti, Elvis & Nicastro 2002; Markowitz, Krumpe & Nikutta 2014) characterized by a distribution of a large number of individual clouds.

Since the first detection of resonance iron K shell absorption lines blueshifted to rest-frame energies of $E > 7$ keV in luminous AGNs (Chartas, Brandt & Gallagher 2003; Pounds et al. 2003; Reeves, O'Brien & Ward 2003), high velocity outflows have become an essential component in the overall understanding of AGNs. The faster components of these winds are thought to occur as a result of the accretion process and originates in the inner regions near the black hole whereas the warm absorbers at lower velocities probably originate from much further out e.g. > 10 pc and greater (e.g. Blustin et al. 2005; Reeves et al. 2013). Fast disc-winds are present in ∼40 per cent of the bright AGNs (Tombesi et al. 2010; Gofford et al. 2013), suggesting that their geometry is characterized by a wide opening angle, as confirmed in the luminous quasar PDS 456 by Nardini et al. (2015). These winds are considered the key ingredient of AGN feedback models and might represent the missing link in the observed galactic feedback process, by driving massive molecular outflows out to large (∼kpc) scales in galaxies (Cicone et al. 2014; Feruglio et al. 2015; Tombesi et al. 2015; Cicone et al. 2018).

Disc-winds are characterized by a high column density ($N_{\rm H} \sim 10^{23}$ cm^{-2}) and a mean velocity $\langle v_{\rm w} \rangle \sim 0.1c$ (Tombesi et al. 2010). These high velocities can result in a large amount of mechanical power, possibly exceeding the 0.5–5 per cent of the bolometric luminosity ($L_{\rm bol}$), suggesting a significant AGN feedback contribution to the evolution of the host galaxy (King 2003; King & Pounds 2003; Di Matteo, Springel & Hernquist 2005; Hopkins &

★ E-mail: gabriele.matzeu@sciops.esa.int (GAM); valentina.braito@brera.inaf.it (VB)

Elvis 2010; Tombesi et al. 2015). However, the velocity of the Fe K absorbers can span over a wide range, from as low as a few $\times 100-1000\,\mathrm{km\,s^{-1}}$ (more typical of what is seen in the soft X-ray warm absorbers; e.g. Kaastra et al. 2000; Blustin et al. 2005; Reeves et al. 2013) up to mildly relativistic values of $\sim 0.2-0.4c$ in the most extreme cases (e.g. Chartas et al. 2002; Reeves et al. 2009; Parker et al. 2017, 2018. A recent simultaneous *XMM–Newton* and *NuSTAR* observation of the luminous quasar PDS 456 carried out in March 2017 revealed a new relativistic component of the fast wind while observed in the low-flux state (Reeves et al. 2018), which provided the evidence of the multiphase structure disc-wind. In recent studies, a positive correlation was also found between the outflow velocity of the disc-wind and the X-ray luminosity in PDS 456 (Matzeu et al. 2017) and IRAS 13224–3809 (Pinto et al. 2018), which is what is expected in a radiatively driven wind scenario.

MCG–03–58–007 is a nearby ($z = 0.0315$) bright Seyfert 2 galaxy. It was first selected as a Compton-thick AGN (i.e. $N_{\rm H} > 10^{24}\,\mathrm{cm^{-2}}$) candidate due to its faint X-ray flux (Severgnini, Caccianiga & Della Ceca 2012) as measured in a 10 ks observation with *XMM–Newton* in 2005. A longer 80 ks *Suzaku* observation in 2010 revealed an obscured AGN but in the Compton-thin (i.e. $N_{\rm H} \sim 10^{23}\,\mathrm{cm^{-2}}$) regime with two deep blueshifted absorption troughs between 7.5 and 8.5 keV (Braito et al. 2018, B18 hereafter). These are associated with two zones of a highly ionized ($\log(\xi/\mathrm{erg\,cm\,s^{-1}}) \sim 5.5$) disc-wind with column density of $\log(N_{\rm H}/\mathrm{cm^{-2}}) \sim 23.7$ and $\log(N_{\rm H}/\mathrm{cm^{-2}}) \sim 23.9$, and outflowing at a mildly relativistic speed of $v_{\rm w} \sim 0.1$–$0.2c$. A more recent 130 ks simultaneous *XMM–Newton* and *NuSTAR* observation confirmed the presence of the wind and showed a rapid $N_{\rm H}$ variation on a time-scale of $\sim$1 d (B18). Such short-term variability suggests the presence of inhomogeneous material as part of the disc-wind, rapidly crossing the line of sight. The work presented in B18 was focused on the analysis of the hard X-ray band and on the detection of the blueshifted iron K absorption features in MCG–03–58–007.

The main motivation of this follow-up paper is to undertake a full broad-band analysis of MCG–03–58–007 with the simultaneous *XMM–Newton* and *NuSTAR* data by parametrizing the observation with a more physically motivated model for the neutral absorber such as `MYTorus` (Murphy & Yaqoob 2009). With this comprehensive broad-band analysis we can (a) investigate whether the spectral variability, as seen through the hardening of the spectra, is to a change in the clumpy neutral absorber or to an inhomogeneous highly ionized disc-wind; (b) to investigate in detail, for the first time in this source, the physical properties of the soft X-ray emission. This paper is organized as follows: in Section 2, we summarize the data reduction, whereas in Section 3 we describe the spectral analysis that focuses on the RGS spectra. In Section 4, we focus on the broad-band spectral analysis of the simultaneous *XMM–Newton* and *NuSTAR* observation of MCG–03–58–007 which includes a time-dependent spectral analysis. In Section 5, we discuss the possible origin of the observed soft X-ray emission lines and we discuss whether the obscuration event is caused by a transiting neutral absorber or by an inhomogeneous highly ionized disc-wind. In Section 5, we also discuss the energetic and location of the highly ionized absorber and compare it with what was found in B18.

In this paper, the values of $H_0 = 70\,\mathrm{km\,s^{-1}\,Mpc^{-1}}$ and $\Omega_{\Lambda_0} = 0.73$ are assumed throughout and errors are quoted at the 90 per cent confidence level ($\Delta\chi^2 = 2.71$ and $\Delta C = 2.71$) for one parameter of interest unless otherwise stated.

2 OBSERVATIONS AND DATA REDUCTION

XMM–Newton observed MCG–03–58–007 simultaneously with *NuSTAR* between the 6th and 9th of 2015 December with an exposure time of $\sim$130 ks (see Table 1). The *NuSTAR* observation started approximately 2 h before the *XMM–Newton* one and ended 150 ks afterwards (see Table 1), with a total duration of 281.8 ks. All the *XMM–Newton* data were reduced by adopting the Science Analysis System (SAS v16.0.0). The most recent set of calibration files and the EPIC-pn and MOS 1 + MOS 2 adopted in this work are the same used in B18. The same applies for the *NuSTAR* data, reduced according to the *NuSTAR* Data Analysis Software package (NUSTARDAS v1.6.0). The *XMM–Newton* RGS data have been reduced by using the standard SAS task *rgsproc*, where the high background time intervals were filtered out by applying a threshold of $0.2\,\mathrm{cts\,s^{-1}}$ on the background event files. After checking that the RGS 1 and RGS 2 spectra were in good agreement, to within the 3 per cent level, we combined them by using the SAS task *rgscombine*. The two combined RGS collected a total of 411 net counts. Due to the low number of net counts, the spectra were binned to $\Delta\lambda = 0.1$Å which undersamples the RGS FWHM spectra resolution of $\Delta\lambda = 0.06$–0.08Å. At this binning, the spectra are characterized by <20 counts per channel and hence we adopted C-statistics (Cash 1979) in the RGS analysis, whereas we adopt χ^2 minimization technique for the EPIC and FPMA/B spectral analysis. All the models adopted were fitted to the data by using the standard software package XSPEC v12.9.1p (Arnaud 1996).

In Fig. 1, we show the time-averaged pn, MOS 1 + 2 and FPMA/B spectra plotted with the corresponding X-ray background (binned to 3σ for clarity) between the 0.3 and 70 keV rest energy band. In the soft band, the EPIC data were filtered for high background which severely affected the observation (as reported in B18) while in the hard X-ray band the background dominates above 50 keV. After screening, the background level is only $\sim$5–10 per cent of the net source rate for the pn and the combined MOS. In the broad-band fitting we will confront different physical reprocessing scenarios including the `MYTorus` model (Murphy & Yaqoob 2009), which is valid at $E > 0.6$ keV and hence for the rest of the broad-band analysis we concentrate on the 0.6–50 keV band. A Galactic absorption column of the $N_{\rm H} = 2.5 \times 10^{20}\,\mathrm{cm^{-2}}$ (Dickey & Lockman 1990), as from the H I 21 cm measurements, was adopted in all the fits and we also assume solar abundance of the main abundant elements throughout the analysis.

3 SOFT X-RAY SPECTRAL ANALYSIS

As already shown in B18, both the *Suzaku* and *XMM–Newton* soft ($E < 2$ keV) spectra are rich in emission lines. This is also evident in Fig. 2 where we show the 0.5–1.5 keV residuals for the *XMM–Newton* EPIC data (black and red lines are the pn and MOS spectra, respectively). The adopted model is a simple power-law and Galactic absorption. Since this line-dominated soft spectral range could reveal information on the circumnuclear gas surrounding the AGNs, we analysed the high-resolution spectrum collected with the RGS. In particular, we considered the RGS spectrum between 0.38–2 keV (6.20–32.63 Å) in order to build a template for the soft X-ray emission which we later apply to the broad-band and the time-dependent spectral analysis in Section 4.

Table 1. Summary of the 2015 simultaneous *XMM–Newton* and *NuSTAR* observation of MCG–03–58–007.

	XMM–Newton			*NuSTAR*	
Obs. ID		0764010101		60101027002	
Instrument	PN	MOS 1+MOS 2	RGS 1+RGS 2	FPMA	FPMB
Start date, time (UT)	2015-12-06, 12:56:06	2015-12-06, 12:33:16	2015-12-06, 13:33:07	2015-12-06, 10:36:08	2015-12-06, 10:36:08
End date, time (UT)	2015-12-08, 01:25:11	2015-12-08, 01:29:12	2015-12-08, 01:33:25	2015-12-09, 17:21:08	2015-12-09, 17:21:08
Duration (ks)	131.3	258.0	266.4	281.8	282.8
Exposure(ks)[a]	59.9	195.3	213.1	131.4	132.0
$Flux_{(0.5-2)keV}$[b]	0.0877	0.0879	0.0927	–	–
$Flux_{(2-10)keV}$[b]	1.95	1.94	–	1.57	1.63
$Flux_{(3-50)keV}$[b]	–	–	–	4.93	5.12

[a]Net exposure time, after background screening and dead-time correction.
[b]Observed fluxes in the 0.5–2, 2–10, and 3–50 keV bands in units $\times\ 10^{-12}$ erg cm^{-2} s^{-1}.

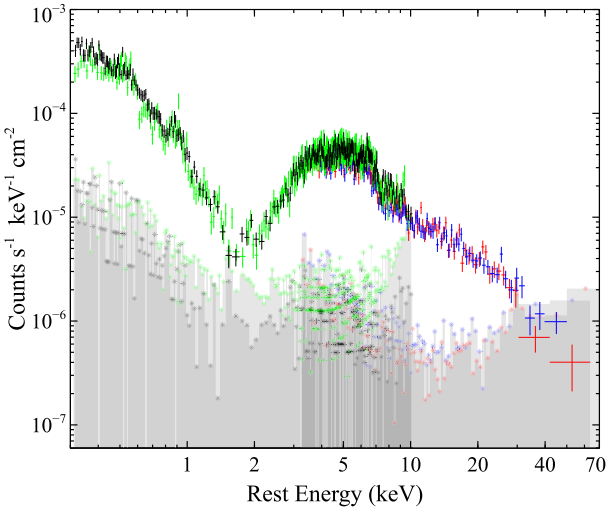

Figure 1. Time-averaged background-subtracted source and the time-averaged background spectra of the simultaneous *XMM–Newton* and *NuSTAR* observation of MCG–03–58–007. The net spectra shown here are the pn (black), MOS 1 + 2 (green), FPMA (red), and FPMB (blue) where the relative background spectra are all plotted with the corresponding colours and clearly dominate above 50 keV. This data have been binned to 3σ for clarity.

3.1 RGS analysis

As a first step, the RGS spectrum was fitted with a simple power-law (`zpowerlaw`) and a Galactic absorption model (`Tbabs` with cross-section and ISM abundances of Wilms, Allen & McCray 2000). This simple continuum model returned a photon-index of $\Gamma \sim 2.4$ which is broadly consistent with that found in the broad-band analysis in Section 4. Since the residuals in the spectrum suggests the presence of multiple unresolved narrow emission lines, we modelled them with Gaussian components (`zgauss`) in XSPEC, with the line-width fixed at $\sigma = 1$ eV. We note that, the inclusion of a line requires to provide an improvement of $\Delta C \geq 4.6$ for two free parameters (i.e. line energy and the normalization) corresponding to a ≥ 90 per cent confidence level. Following this criterion we formally detected 11 emission lines, 10 of which have a secure identification mostly associated, in their rest frame, with He- and H-like of abundant elements such as N, O, and Ne. There is an additional line at 618^{+1}_{-2} eV (or 20.10 Å) which does not correspond to a known transition. Two additional emission lines where marginally detected ($\Delta C/\Delta\nu < 4.6/2$) at the expected rest-frame energies of $E = 574^{+1}_{-2}$ eV (21.60 Å) and $E = 1884^{+27}_{-23}$ eV (6.58 Å) which can be associated with the resonance transition of O VII and Si XIII, respectively.

The overall fit statistic considerably improved upon the addition of the Gaussian line profiles decreasing from $C/\nu = 407/289$, without any line emissions (null hypothesis probability 2.6×10^{-5}) to a more statistically acceptable $C/\nu = 298/263$ (null hypothesis probability 9.8×10^{-2}) with the included lines. Fig. 3 shows the rest-frame 6–30 Å RGS spectrum with the best-fitting model (red lines) overlaid on. The emission line fluxes, equivalent widths (*EW*) and identifications are listed in Table 2. The centroid energy of the O VII line at the rest energy of $E = 562 \pm 1$ eV (22.06 Å) suggests an identification with the forbidden transition, detected at 3σ confidence level. The intercombination transition is also detected at the expected energy of $E = 569 \pm 2$ eV (21.79 Å) but with a lower significance at the $\sim 2\sigma$ level.

As for the other He-like complexes such as the N VI and Ne IX triplets, we only observed the forbidden component at the expected energy of $E = 419 \pm 1$ eV (29.59 Å) and $E = 906^{+2}_{-3}$ eV (13.69 Å). Although the RGS spectrum has a low number of counts, we can observe that the soft X-ray emission lines are largely dominated by forbidden transitions rather than resonance and/or intercombination emission (see Fig. 3).

This result suggests that such emission line mainly originates from a distant low-density photoionized plasma as seen in many Seyfert 2s (e.g. Sako et al. 2000; Kinkhabwala et al. 2002; Kallman et al. 2014). In particular, a strong emission line well match with the O VIII Lyα emission at the expected rest frame energy of $E = 653^{+2}_{-1}$ eV (18.99 Å). The line width estimate ($\sigma < 3.7$ eV) corresponds to an upper limit on the velocity of $\sigma_v \lesssim 1700$ km s^{-1} (FWHM $\lesssim 4000$ km s^{-1}) and hence broadly consistent with emitting gas possibly located in the BLR/NLR.

A possible diagnostic for the density of the emitting gas can be carried out by quantifying the ratio between the intensity of the forbidden and intercombination components detected in He-like triplets (Porquet & Dubau 2000). However in this work, the only possible diagnostic can be carried out on the O VII Heα lines as this is the only triplet detected. The resulting emission line ratio is $R = z/(x + y) = 3.7^{+1.6}_{-0.8}$ (where z and $x + y$ are the forbidden and intercombination transition, respectively). This ratio places an upper limit on the electron density of the order of $n_e < 2 \times 10^9$ cm^{-3} (see fig. 8 of Porquet & Dubau 2000). Nevertheless, the spectral resolution in the RGS does not allow to put accurate constraints on the widths and location of these lines. The above estimates suggests that the lines could be, in principle, broad and emitted from a gas with a density lower than $\times 10^9$ cm^{-3} and hence located at $R_{gas} \gtrsim$ BLR.

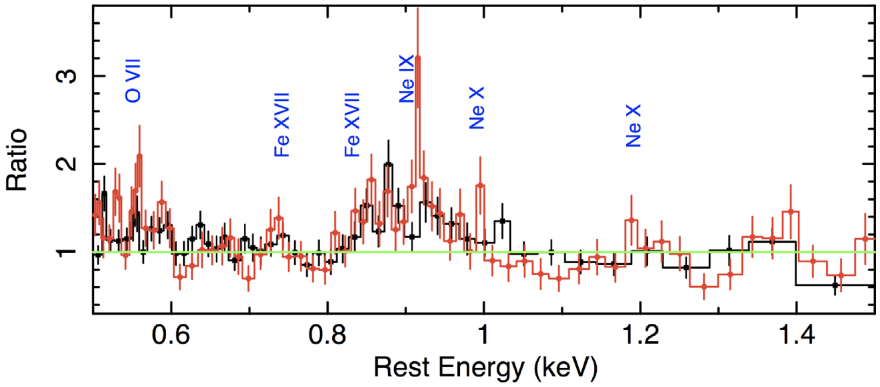

Figure 2. Data/model ratio for the pn (black) and the combined MOS (red) spectra between 0.5–1.5 keV. The adopted model is a simple power-law and Galactic absorption. We note that although MCG–03–58–007 is faint and absorbed in the soft X-ray band, its emission is largely line-dominated.

Furthermore, all the detected soft emission lines are consistent to their expected rest-frame energies, except N VII Lyα line which lies slightly above it (see Table 2). The possible emission line detected at $E = 729^{+1}_{-2}$ eV (17.01 Å), has an uncertain identification but it could be associated with an L-shell transition from iron (e.g. Fe XVII 3s $\rightarrow$ 2p). A contribution from the radiative recombination continuum of O VII is also plausible. Another strong iron L emission is identified at rest energy of $E = 828^{+2}_{-3}$ eV (14.97Å), which lies very close to the expected rest-frame energy of Fe XVII 3d $\rightarrow$ 2p transition. The iron L transitions are associated with collisionally ionized plasma, likely within the star-forming regions in the host galaxy.

Having reached a good parametrization of the narrow emissions with the Gaussian profiles, we subsequently replaced the Gaussian emission line fit with a publicly available XSTAR photoionization emission grid[1] (Bautista & Kallman 2001). Despite the low number of counts in the RGS, the inclusion of the XSTAR grid can provide a first-order estimate on the physical condition of the gas such as ionization, column and electron density. As the emission profiles appear to be narrow, we chose a suitable grid with velocity broadening of $v_{\rm turb} = 100\,{\rm km\,s^{-1}}$. Moreover, we find that in order to model it with XSTAR, it is preferable to adopt a larger binning (i.e. $\Delta\lambda = 0.2$ Å) to the spectrum.

From the photoionization modelling, the XSTAR emission flux (or normalization) is expressed as

$$\kappa_{\rm xstar} = f_{\rm cov}\frac{L_{38}}{D^2_{\rm kpc}}, \quad (1)$$

where L_{38} is the ionizing luminosity ($L_{\rm ion}$) in units of $10^{38}\,{\rm erg\,s^{-1}}$, $D_{\rm kpc}$ is the luminosity distance of the ionizing source (AGN) in kiloparsecs, and $f_{\rm cov} = \Omega/4\pi$ is the covering fraction of the gas. Thus, by keeping the $N_{\rm H}$ fixed to the default value given in the XSTAR table of $\log(N_{\rm H}/{\rm cm^{-2}}) = 21.5$, which is more typical of a diffused warm emission component found in Seyfert 1 and Seyfert 2s galaxies (e.g. Kinkhabwala et al. 2002; Blustin et al. 2005), we get a normalization of $\kappa_{\rm xstar} = 1.2^{+0.4}_{-0.4} \times 10^{-6}$. By assuming a bolometric luminosity in MCG–03–58–007 of $L_{\rm bol} \sim 3 \times 10^{45}\,{\rm erg\,s^{-1}}$ (B18) and that $L_{\rm ion} \sim L_{\rm bol}/3 \sim 10^{45}{\rm erg\,s^{-1}}$, at a luminosity distance of $D_{\rm L} = 138.8$ Mpc, we obtain a corresponding gas covering fraction of the order of $\sim$0.2 per cent. This suggests that the distant photoionized gas is covering a small fraction of the sky and possibly inhomogeneous, however this result is strongly dependent on a given column density. If we assume a 10 per cent covering factor, which is broadly expected in the NLR (e.g. Netzer & Laor 1993), it would require a normalization of $\kappa_{\rm xstar} = 5.2 \times 10^{-5}$ corresponding to a column density of $\log(N_{\rm H}/{\rm cm^{-2}}) = 19.9^{+0.1}_{-0.2}$.

The ionization state of the plasma was measured to be $\log(\xi/{\rm erg\,cm\,s^{-1}}) = 1.18^{+0.22}_{-0.27}$ and the addition of the photoionized gas emission component results in a considerable improvement to the overall fit to $\Delta C/\Delta\nu = 34.2/2$ which is at > 99.99 per cent confidence level. This is somewhat expected considering that the soft X-ray emission is dominated by forbidden transitions. The inclusion of a thermal component via the XSPEC (MEKAL; Mewe, Gronenschild & van den Oord 1985) model, led a modest improvement in the fit statistic of $\Delta C/\Delta\nu = 8.5/2\,(2.5\sigma)$. Here, we find a poorly constrained temperature of $kT = 0.35^{+0.25}_{-0.15}$ keV and a normalization of $1.5^{+0.4}_{-0.9} \times 10^{-5}\,\frac{10^{-14}}{4\pi[D_{\rm A}(1+z)]^2}\int n_{\rm e} n_{\rm H} {\rm d}V$, where $n_{\rm e}$ and $n_{\rm H}$ are the electron and hydrogen densities (measured in ${\rm cm^{-3}}$), respectively and $D_{\rm A}$ is the angular diameter of the source in cm. Lastly, we kept the photon-index of the soft power-law component fixed at the best value, found in B18 and later in the broad-band analysis of $\Gamma = 2.2$. Note that with such a complex model, the normalization of the scattered power-law component is no longer well constrained. In Fig. 4, we show the best-fitting model (red) to the data with the corresponding contribution of both thermal (green) and photoionized (blue) components. The latter clearly dominate across the RGS spectrum.

4 BROAD-BAND *XMM–Newton* AND *NuSTAR* ANALYSIS

4.1 Description of the *XMM–Newton* & *NuSTAR* light curves

In Fig. 5, we show the *XMM–Newton* (blue) and *NuSTAR* (red) light curves in different energy bands, as well as the hardness ratio between the 6–10 and 20–40 keV bands observed by *NuSTAR*. The light curve in the 0.5–2 keV band shows no variability while the flux in the 3–6 keV band in particular drops strongly at around 125 ks, from $\sim$11 to $\sim$0.04 cts s^{-1}, after the start of the *NuSTAR* observations. In comparison, the 20–40 keV hard X-ray band shows little variation throughout the observations. Indeed the ratio between the 20–40 and 3–6 keV bands shows a clear increase in hardness at this point, which B18 earlier interpreted as an obscuration event which occurs within an approximate time-scale of one day. Then at the end of the observation at 250 ks, the source flux gradually starts to recover in the remaining 30 ks of the *NuSTAR* observation.

[1] ftp://legacy.gsfc.nasa.gov/software/plasma_codes/xstar/xspectables/

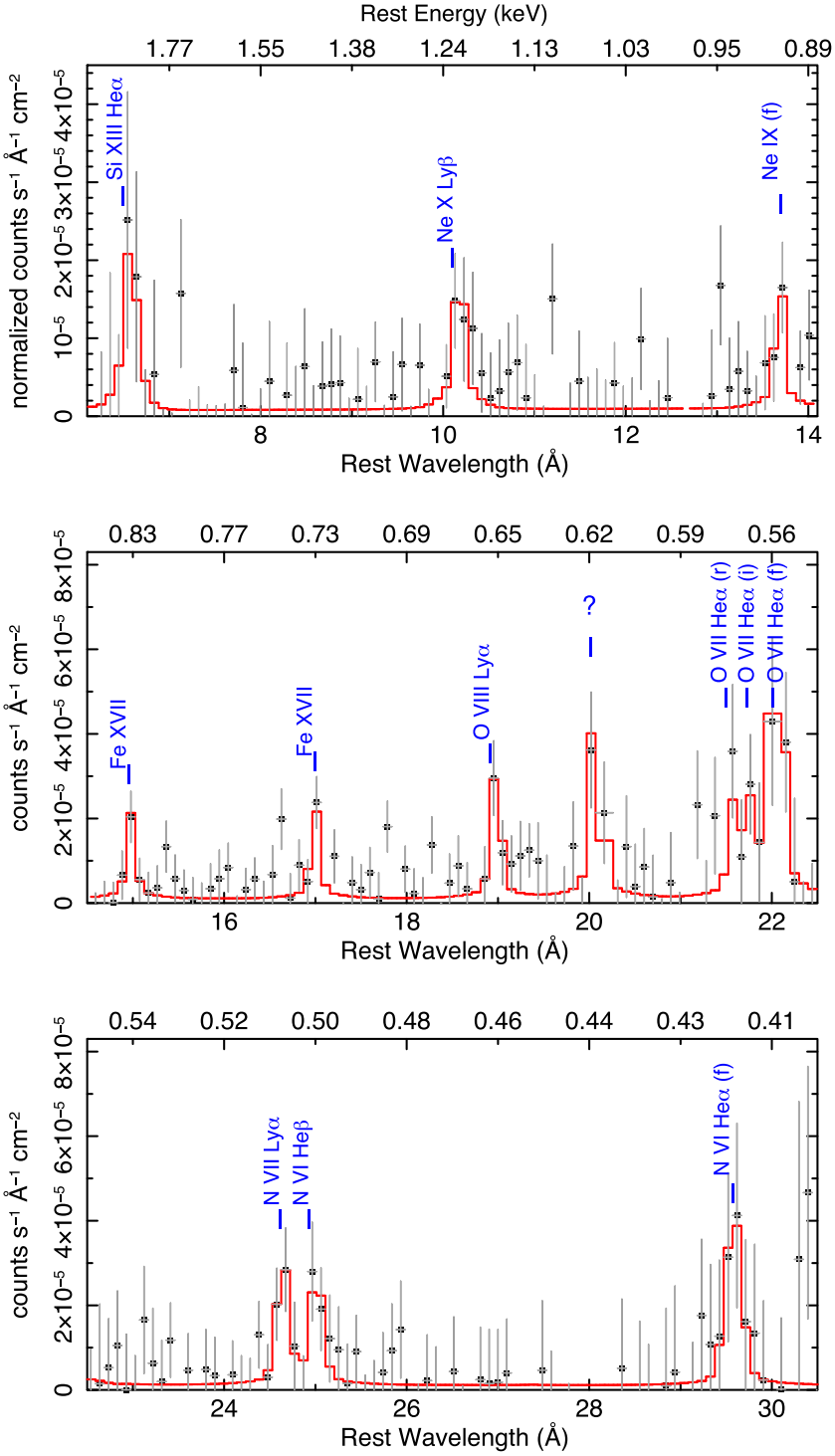

Figure 3. Enlarged view of the combined RGS data of MCG–03–58–007 showing the count rate spectrum normalized to the instrumental effective area. The best-fitting model is shown by the red line. Despite the low number of counts, it was possible to detect 11 emission lines. Ten out of 11 lines were formally identified with the most likely He- and H-like transitions from N, O, and Ne. From the plot it is evident that the forbidden transitions are dominating the spectrum over the resonance and intercombination, suggesting the low-density nature of the photoionized distant gas. The emission line significantly detected at rest energy of $E \sim 620$ eV (~ 20 Å) could not be identified. Two additional emission lines were marginally detected at the rest-frame energies of $E = 574^{+1}_{-2}$ eV (21.60 Å) and $E = 1884^{+27}_{-23}$ eV (6.58 Å), which are identified to the resonance transitions of O VII and Si XIII, respectively.

Accordingly to this behaviour and following B18, the observations were split into three time intervals; from 0 to 125 ks (slice A), 125 to 250 ks (slice B), and 250 to 280 ks (slice C), as marked by vertical dotted lines in Fig. 5. Slice A has a high count rate and is largely coincident with the whole of the *XMM–Newton* observation. On the other hand, in slice B captures the increase in hardness of the source, where in particular the 3–6 keV band count rate drops compared to the 20–40 keV light curve. Note that slice B includes

Table 2. Summary of the emission lines in the RGS spectra from the best-fitting Gaussian model. Note that all the lines are practically unresolved and hence we assume a $\sigma = 1$ eV during fitting.

E_{obs} (1)	Flux (2)	*EW* (3)	Transition (4)	E_{lab} (5)	$\Delta C/\Delta\nu$ (6)
419^{+1}_{-1} [29.59]	$14.7^{+9.2}_{-9.9}$	133^{+83}_{-89}	N VI He α (f)	420	7.0/2
496^{+1}_{-2} [25.00]	$7.0^{+4.4}_{-3.8}$	30^{+19}_{-16}	N VI He β (f)	495	11.0/2
503^{+1}_{-1} [24.65]	$7.5^{+3.7}_{-3.3}$	35^{+17}_{-15}	N VII Lyα	500.4	14.3/2
562^{+1}_{-1} [22.06]	$18.6^{+10.2}_{-10.0}$	78^{+43}_{-42}	O VII He α (f)	561	11.1/2
569^{+2}_{-2} [21.79]	$5.0^{+4.9}_{-3.7}$	10^{+9}_{-7}	O VII He α (i)	568.7	4.8/2
618^{+1}_{-2} [20.10]	$12.1^{+6.6}_{-6.5}$	229^{+124}_{-123}	?	?	10.0/2
653^{+2}_{-1} [18.99]	$6.3^{+2.9}_{-2.7}$	169^{+78}_{-72}	O VIII Lyα	653.7	13.8/2
729^{+1}_{-2} [17.01]	$4.2^{+2.0}_{-1.7}$	145^{+69}_{-59}	Fe XVII 3s $\rightarrow$ 2p	727.1	16.1/2
828^{+2}_{-3} [14.98]	$3.8^{+1.8}_{-1.7}$	179^{+87}_{-81}	Fe XVII 3d $\rightarrow$ 2p	825.8	14.4/2
906^{+2}_{-3} [13.69]	$3.2^{+1.8}_{-1.8}$	186^{+108}_{-104}	Ne IX He α (f)	905.1	8.7/2
1219^{+5}_{-14} [10.17]	$4.0^{+2.2}_{-2.1}$	460^{+260}_{-253}	Ne X Lyβ	1211	9.2/2

Note: (1) Measured line energy in the quasar rest frame, in units of eV where the corresponding mean wavelength value in units of Å is given within the brackets, (2) line photon flux, in units of 10^{-6} cm^{-2} s^{-1}, (3) the equivalent width in the AGN rest frame in units of eV, (4) list of the most plausible identification where (f), (i), and (r) refer to forbidden, intercombination, and resonance transitions for He-like species, (5) corresponding laboratory energy for the detected lines, in units of eV, (6) improvement of the fit in C–statistics upon adding the line to the model.

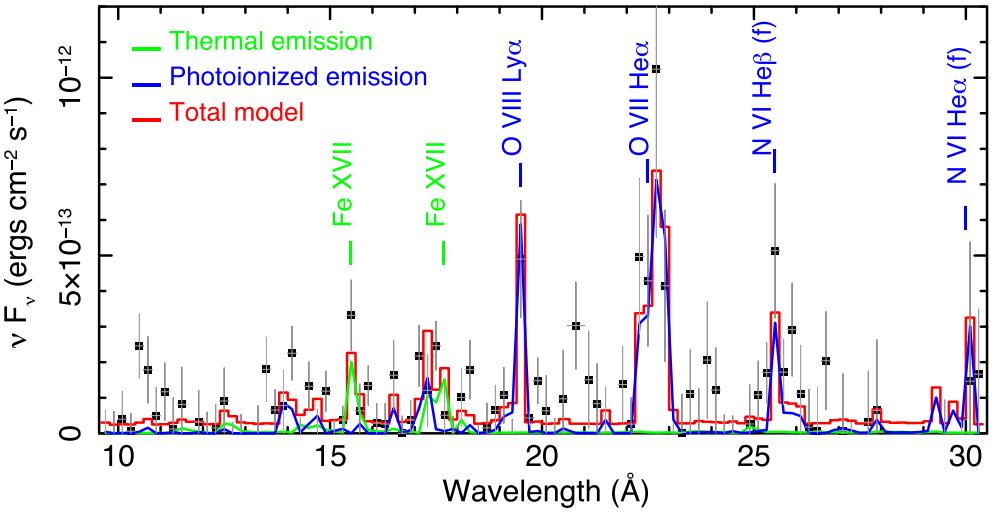

Figure 4. Best-fitting model (red) overlaid on the RGS spectrum with group $\Delta\lambda = 0.2$ Å for extra clarity. The corresponding contribution of both thermal (green) and photoionized (blue) components are shown, where the former is responsible for the collisionally ionized Fe L emission between 15 and 17Å and the latter mainly responsible to all the forbidden transition emission e.g. N VI and O VII He α. The RGS spectrum is clearly dominated by emission from photoionized elements from distant gas possibly located in the NLR.

less than 10 ks of *XMM–Newton* data, which is only included to constrain the soft band spectrum, below 3 keV. In slice C the hardness ratio drops again whereas the source brightness appears to recover. Slice C only consists of *NuSTAR* data between 250 and 280 ks and the spectral properties are intermediate between slice A and slice B. As the quality of spectrum for slice C is low (with only ∼30 ks of net exposure for both *NuSTAR* FPM detectors combined), we do not include this in our subsequent quantitative analysis and thereafter concentrate on slice A and slice B. None the less, the overall variability provides important physical constraints, which as suggested by B18, indicates that the AGN went through an absorption event in order to account for the rapid change in hardness ratio.

4.2 Broad-band analysis of slice A

For the initial broad-band analysis we consider slice A rather than the time-averaged spectra as the former includes the only time-interval where both telescopes are effectively observing simultaneously (see Fig. 5). Since we obtained a reasonable fit with XSTAR and MEKAL in the RGS (see Section 3.1), we adopt the same best-fitting values in the EPIC broad-band spectra. This was achieved by fixing the ionization parameter and by letting the corresponding normalizations readjust accordingly including the temperature of the MEKAL component.

In this work, we adopt two main models. Model $\mathcal{A}$ represents a more classical model where the primary continuum is modelled as power-law component transmitted through a neutral absorber.

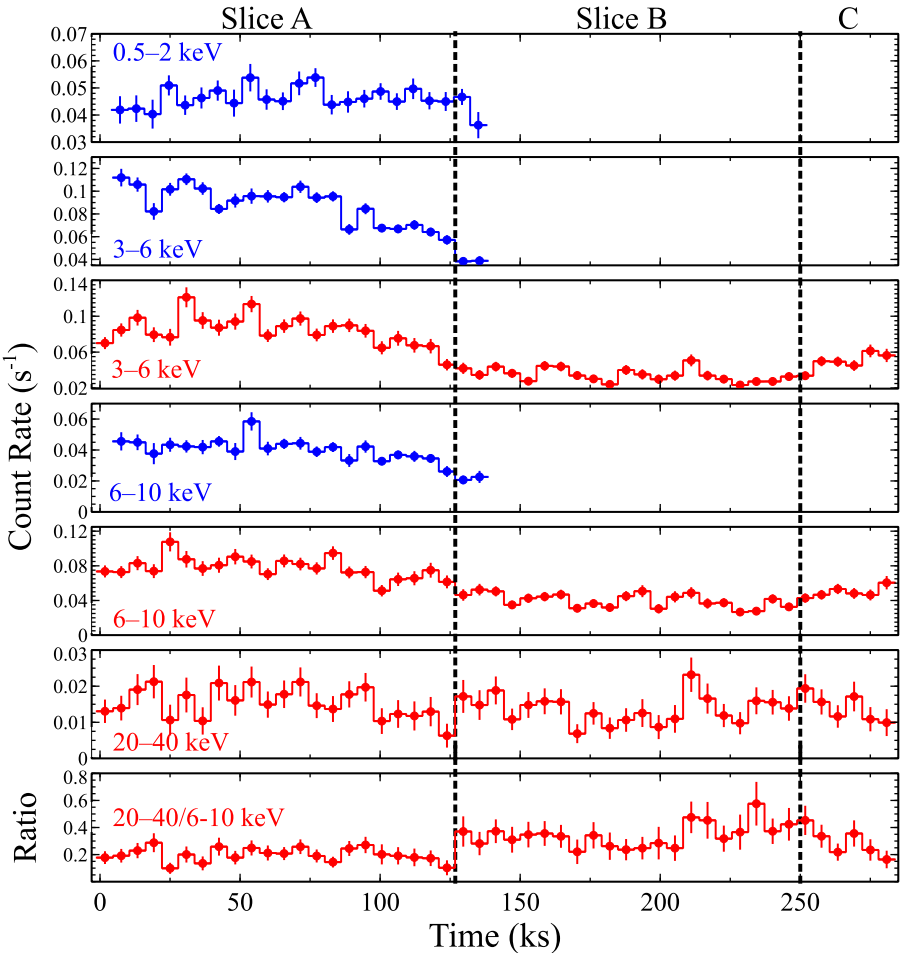

Figure 5. Light curve in different energy bands (i.e. 0.5–2, 3–6, 6–10, and 20–40 keV) corresponding to EPIC-pn (blue) and FPMA+B (red) both binned at 5814 s (one *NuSTAR* orbit), respectively. The hardness ratio between 20–40 and 6–10 keV corresponding to the FPMA+B is plotted on the bottom panel. MCG–03–58–007 was observed simultaneously with *XMM–Newton* and *NuSTAR*, the duration of the latter extended 150 ks beyond *XMM–Newton* to 281.8 ks. According to the behaviour of the light curves, the *XMM–Newton* and *NuSTAR* spectra were sliced in three segments named slice A–C which are visually marked on the plot by the vertical black dotted lines. Thus, slice A and slice B are characterized by the *XMM–Newton* (pn and MOS 1 + 2) and *NuSTAR* (FPMA+B) spectra separated at 0–125 and 125–250 ks, respectively. However, in slice B we are only left with less than 10 ks of *XMM–Newton* data which implies that the *XMM–Newton* contribution will be only from a short EPIC-pn spectrum. Furthermore, slice C is entirely consisting of *NuSTAR* data between 250 and 280 ks.

The Compton reflected component is produced by a distant neutral reflector which is geometrically approximated as a slab of neutral material with `pexmon` (Nandra et al. 2007), whilst a distant scattered continuum component is also included throughout. Model $\mathcal{B}$ assumes a geometrically toroidal reproccesor modelled with `MYTorus` (Murphy & Yaqoob 2009), assuming a standard (coupled) configuration, which takes into account the physical properties of the absorbing medium, the Compton-down scattering effect and it includes self-calculated reflected components (continuum plus Fe K emission lines). This model also assumes a fixed geometry of the toroidal X-ray reprocessor, a single value for the covering factor of the torus (corresponding to a half–opening angle of 60°) and a uniform composition of the torus itself. Model $\mathcal{B}$ will be described in Section 4.2.1. In the following we adopt model $\mathcal{A}$, defined as

$$\begin{aligned}\text{Model } \mathcal{A} = {} & \texttt{Tbabs} \times [\texttt{zpowerlw}_{\rm scatt} + \texttt{xstar}_{\rm em} + \texttt{mekal} \\ & + \texttt{pexmon} + (\texttt{xstar}_{\rm FeK,1} \times \texttt{xstar}_{\rm FeK,2}) \\ & \times \texttt{zpowerlw}_{\rm intr} \times \texttt{zphabs}],\end{aligned}$$

where `Tbabs` accounts for the Galactic absorption, the scattered power-law component is parametrized with $\texttt{zpowerlw}_{\rm scatt}$. $\texttt{zpowerlw}_{\rm intr}$ models the primary continuum which is absorbed by fully covering neutral material (`zphabs`) with a column density of $\log(N_{\rm H}/{\rm cm}^{-2}) = 23.38 \pm 0.02$. The Compton reflection component is modelled with `pexmon` (Nandra et al. 2007) which includes the power-law continuum reflected from distant neutral material and the emission from Fe Kα, Fe Kβ, Ni Kα and Fe K Compton shoulder. The photon-indexes of the reflected and primary continuum components are assumed to be the same, the inclination angle was fixed as 60° (0° corresponds to face-on), and the cut-off energy was 300 keV. The normalization was allowed to vary and the scaling reflection factor parameter was fixed at $R = \Omega/2\pi = 1$.

B18 detected in the *XMM–Newton* and *NuSTAR* spectra two strong absorption features at rest frame energies of 7.4 ± 0.1 and 10.2 ± 0.1 keV associated with blueshifted 1s $\rightarrow$ 2p transition of Fe XXV and Fe XXVI. These absorption profiles likely correspond to two zones of highly ionized outflowing absorbers with velocities

of $v_w \sim -0.1c$ and $v_w \sim -0.3c$. Since the parametrization with the Gaussian absorption profiles has been already explored in B18, here we simply model these features with two multiplicative grids of photoionized absorbers generated with XSTAR photoionization code (v2.21bn13, Kallman et al. 2004), defined as $\texttt{xstar}_{\rm Fe\,K,1}$ and $\texttt{xstar}_{\rm Fe\,K,2}$ respectively. Since these lines are broad, we adopt for all the subsequent fits the original grid used for PDS 456 (Nardini et al. 2015; Matzeu et al. 2016) with a high velocity broadening of $v_{\rm turb} = 10\,000\,{\rm km\,s^{-1}}$. In generating this grid, it was also assumed an intrinsically steep ionizing continuum of $\Gamma = 2.4$, which is consistent with what found in MCG–03–58–007. We find that the addition of two absorption zones with outflow velocities of $v_w/c = -0.09 \pm 0.02$ and $v_w/c = -0.35 \pm 0.02$ and column density of $\log(N_{\rm H}/{\rm cm^{-2}}) = 23.2 \pm 0.1$ and $\log(N_{\rm H}/{\rm cm^{-2}}) = 24.0^{+0.3}_{-0.2}$ improved the fit by $\Delta\chi^2/\Delta\nu = 28.8/3$ (4.7σ) and $\Delta\chi^2/\Delta\nu = 19.9/3$ (3.7σ) for zone 1 and zone 2, respectively. The slower zone prefers a lower ionization ($\log(\xi/{\rm erg\,cm\,s^{-1}}) = 5.4 \pm 0.2$) than the faster zone ($\log(\xi/{\rm erg\,cm\,s^{-1}}) = 6.2^{+0.4}_{-1.0}$). For the latter zone, the ionization and column density of the ionized absorber are highly degenerate which explains the large error. Here, we note that the *XMM–Newton* and *NuSTAR* spectra are dominated by the transmitted primary absorbed component above $\sim$2 keV. The intensities of the reflected and primary component are ${\rm norm_{pexmon}} = 1.3 \pm 0.5 \times 10^{-3}\,{\rm ph\,cm^{-2}\,s^{-1}\,keV^{-1}}$ and ${\rm norm_{zpow}} = 2.9^{+0.4}_{-0.3} \times 10^{-3}\,{\rm ph\,cm^{-2}\,s^{-1}\,keV^{-1}}$, respectively, which corresponds to a reflection fraction $R = 0.5 \pm 0.1$. Overall model $\mathcal{A}$ provided a good fit to slice A of $\chi^2/\nu = 714/660$. The details of the best-fitting model are listed in Table 3.

In terms of the soft excess, the soft photoionized emission component is modelled with the same XSTAR emission grid ($\texttt{xstar}_{\rm em}$) and the corresponding $N_{\rm H}$ and ξ values used in the RGS. Its normalization is readjusted to a slightly higher measurement (but consistent within the errors found in the RGS) of $\kappa_{\rm xstar} = 1.6^{+0.4}_{-0.5} \times 10^{-6}$. If we let the ionization parameter to be free to vary, the resultant fit would lead to a considerable decrease of ξ from $\log(\xi/{\rm erg\,cm\,s^{-1}}) \sim 1.2$ to $\log(\xi/{\rm erg\,cm\,s^{-1}}) \sim 0.6$. However, if we assume this value in the RGS model it would practically account only for the steep continuum and not model than the individual emission lines. The other contribution to the soft excess is associated with starburst emission which is modelled with a thermal component emission (MEKAL) with a temperature of $kT = 0.79^{+0.05}_{-0.05}$ keV. We find that after including both the thermal and the photoionized components, the photo-index of the scattered continuum is still steep at $\Gamma = 3.3^{+0.9}_{-0.8}$. Note that such steep value cannot be decreased even by adding a second MEKAL component. This might indicate that the scattered soft X-ray power law is steeper than what observed in the hard X-rays. This could be caused by the presence of an intrinsic soft excess as seen in many type 1 AGNs (e.g. Singh, Garmire & Nousek 1985; Turner & Pounds 1988; Nardini et al. 2011).

4.2.1 XMM–Newton *&* NuSTAR *modelling with MYTorus*

In the above fitting, the `pexmon` model assumes geometrically a simple slab reflector. In the following, we replace both the `pexmon` and the simple neutral absorber (`zphabs`) with the `MYTorus` model. It is essentially composed by three tables, developed for XSPEC, of reprocessed spectra (for more details see Murphy & Yaqoob 2009) assuming a primary power-law input spectrum that interacts with a reprocessor with toroidal geometry. We therefore analyse slice A with model $\mathcal{B}$ which is constructed mathematically as follows:

$$\begin{aligned}\text{Model } \mathcal{B} = {} & \texttt{Tbabs} \times [\texttt{zpowerlw}_{\rm scatt} + \texttt{xstar}_{\rm em} + \texttt{mekal} \\ & + A_{\rm S} \times \texttt{MYTorusS} + \texttt{MYTorusZ} \\ & \times (\texttt{xstar}_{\rm FeK,1} \times \texttt{xstar}_{\rm FeK,2}) \times \texttt{zpowerlw}_{\rm intr} \\ & + A_{\rm L} \times \texttt{gsmooth} \times \texttt{MYTorusL}],\end{aligned}$$

where `MYTorusS` and `MYTorusL` are publicly available emission grids that reproduce respectively to the reflected continuum and the Fe Kα, Fe Kβ emission line spectrum. `MYTorusZ` is a multiplicative table corresponding to the zeroth-order transmitted continuum, containing pre-calculated transmission factors that affect the incident continuum due to photoelectric absorption. The `gsmooth` component is a convolution model, available on XSPEC, which takes into account the broadening of the Fe K emission lines. The soft excess and the iron K absorption features have been modelled as in model $\mathcal{A}$ returning consistent values as listed in Table 3.

Here, we constructed `MYTorus` assuming the standard 'coupled' configuration (Yaqoob 2012) which assumes that the angle at which the line of sight directly intercepts the torus is the same (i.e. coupled) as the scattered one. Here, the relative reflected and fluorescence line emitting normalizations are set to be equal to the primary power-law normalization i.e. ${\rm norm_S} = {\rm norm_L} = {\rm norm_{intr\,zpowl}}$, while all the constant factors are set to unity i.e. $A_{\rm S} = A_{\rm L} = 1$. The line-of-sight inclination angle in respect to the polar axis was fixed at its best-fitting value of $\theta_{\rm obs} = 70.0^\circ$, consistent with the type 2 classification. The overall column density measured in this (coupled) configuration indicates that we are viewing the source through Compton thin material i.e. $\log(N_{\rm H}/{\rm cm^{-2}}) = 23.31 \pm 0.01$, which might suggest that the upper regions of the torus are indeed less dense than the more central one. Overall in model $\mathcal{B}$ the transmitted component also dominates over the reflected component above 2 keV. The photo-index was found to be $\Gamma = 2.14 \pm 0.05$ and the normalization of the primary is $2.7 \pm 0.3 \times 10^{-3}\,{\rm ph\,cm^{-2}\,s^{-1}\,keV^{-1}}$. Model $\mathcal{B}$ also provided a very good fit to slice A at $\chi^2/\nu = 719.7/662$ which is comparable to model $\mathcal{A}$.

Fig. 6 shows the best-fitting model $\mathcal{B}$ to slice A and it seems to reproduce quite well the overall spectra. In the following analysis, in Section 4.3 we will only focus on the `MYTorus` model as it assumes a better and a more realistic physical geometry of the reprocessor. In both model $\mathcal{A}$ and model $\mathcal{B}$ adopted here in slice A, the two distinct zones of the wind are ubiquitous, with consistent column densities and outflow velocities (see Table 3).

4.3 Time sliced spectral analysis

From the above broad-band spectral analysis, we show that both models $\mathcal{A}$ and $\mathcal{B}$ successfully fitted slice A. However, B18 detected a rapid spectral variability in MCG–03–58–007 between slice A and slice B which was likely caused by an obscuration event during the *XMM–Newton* and *NuSTAR* observation. In the following we verify whether, by adopting a more self-consistent model for the neutral absorber such as `MYTorus` (model $\mathcal{B}$), rather than a slab reprocessor (model $\mathcal{A}$), the result discussed in B18 is still valid. In particular, we explore whether the obscuration event is caused by (i) a transiting neutral absorber within a clumpy torus or rather is (ii) the result of the inhomogeneous nature of the highly ionized and fast disc-wind where a filament or clump rapidly crosses the line of sight (as also seen in PDS 456 Matzeu et al. 2016). We first attempt to test scenario (i) with model $\mathcal{B}$ by only varying the line-of-sight column density and the primary continuum normalization, whilst keeping the wind parameters tied between the two slices.

Table 3. Summary of the broad-band best-fitting parameters applied for slice A of *XMM–Newton* and *NuSTAR* (see the text for details). [t] and ∗ denote tied and frozen parameters, respectively, during fitting.

Component	Parameter	Model $\mathcal{A}$ (Slab reprocessor)	Model $\mathcal{B}$ (Toroidal reprocessor)
	Continuum		
Primary power-law	Γ	$2.25^{+0.07}_{-0.07}$	$2.14^{+0.05}_{-0.05}$
	norm[a]	$2.9^{+0.4}_{-0.3}$	$2.7^{+0.3}_{-0.3}$
Scattered continuum	Γ	$3.33^{+0.87}_{-0.83}$	2.14^{t}
	norm[b]	$1.3^{+0.4}_{-0.4}$	$1.3^{+0.2}_{-0.2}$
	Soft X-ray emission		
Photoionized[c]	$\log(N_{\rm H}/{\rm cm}^{-2})$	21.5∗	21.5∗
	$\log(\xi/{\rm erg\,cm\,s}^{-1})$[d]	1.2∗	1.2∗
	$\kappa_{\rm xstar}$[e]	$1.6^{+0.4}_{-0.5}$	$1.8^{+0.2}_{-0.2}$
Thermal	kT(keV)	$0.79^{+0.05}_{-0.05}$	$0.78^{+0.04}_{-0.05}$
	norm ($\times\,10^{-5}$)[f]	$1.4^{+0.2}_{-0.2}$	$1.5^{+0.2}_{-0.2}$
	Distant reprocessor and neutral absorber		
`MYTorus`	Γ	–	2.14^{t}
	$\log(N_{\rm H}/{\rm cm}^{-2})$[g]	–	$23.21^{+0.01}_{-0.01}$
	$\log(N_{\rm H,S}/{\rm cm}^{-2})$	–	–
	$\log(N_{\rm H,Z}/{\rm cm}^{-2})$	–	–
	$\rm norm_S = norm_L$	–	2.7^{t}
	$\rm norm_{S00} = norm_{L00} = norm_{S90}$	–	–
`pexmon`	Γ	2.25^{t}	–
	norm[h]	$1.3^{+0.5}_{-0.5}$	–
`zphabs`	$\log(N_{\rm H}/{\rm cm}^{-2})$	$23.38^{+0.02}_{-0.02}$	–
	Highly ionized absorber		
Zone 1[i]	$\log(N_{\rm H}/{\rm cm}^{-2})$	$23.2^{+0.1}_{-0.1}$	$23.2^{+0.1}_{-0.1}$
	$\log(\xi/{\rm erg\,cm\,s}^{-1})$	$5.4^{+0.2}_{-0.2}$	$5.3^{+0.2}_{-0.2}$
	$v_{\rm w}/c$	$-0.09^{+0.02}_{-0.02}$	$-0.09^{+0.02}_{-0.02}$
Zone 2[i]	$\log(N_{\rm H}/{\rm cm}^{-2})$	$24.0^{+0.3}_{-0.2}$	$24.1^{+0.3}_{-0.2}$
	$\log(\xi/{\rm erg\,cm\,s}^{-1})$	$6.2^{+0.4}_{-1.0}$	$6.2^{+0.3}_{-1.0}$
	$v_{\rm w}/c$	$-0.35^{+0.02}_{-0.02}$	$-0.35^{+0.02}_{-0.02}$
Cross-normalization	MOS	0.95 ± 0.02	0.95 ± 0.02
	FPMA	1.07 ± 0.04	1.07 ± 0.04
	FPMB	1.12 ± 0.05	1.12 ± 0.05
Fit statistic	χ^2/ν	714.3/660	719.7/662

[a] Primary power-law normalization in unit of $\times 10^{-3}$ photons cm^{-2} s^{-1} keV^{-1}.
[b] Scattered power-law component in units of $\times 10^{-5}$ ph cm^{-2} s^{-1} keV^{-1}.
[c] `xstar` emission grid with $v_{\rm turb} = 100$ km s^{-1}.
[d] Ionization parameter with fixed value obtained from the RGS fit.
[e] Normalization of the XSTAR emission component, in units of $\times\,10^{-6}$ in terms of $f_{\rm cov}\frac{L/10^{38}}{D^2_{\rm kpc}}$.
[f] Normalization in units of $10^{-5}\,\frac{10^{-14}}{4\pi[D_{\rm A}(1+z)]^2}\int n_{\rm e} n_{\rm H} {\rm d}V$, where $n_{\rm e}$ and $n_{\rm H}$ are the electron and hydrogen densities (measured in cm^{-3}), respectively, and $D_{\rm A}$ is the angular diameter of the source in cm as defined in the MEKAL model.
[g] Mean line-of-sight column density, integrated over all lines of sight through the torus calculated as $(\pi/4)N_{\rm H}$.
[h] ($\times 10^{-3}$ ph cm^{-2} s^{-1} keV^{-1}).
[i] XSTAR absorption grid with $v_{\rm turb} = 10\,000$ km s^{-1}.

However such model simply fails to fully reproduce the curvature in slice B, leaving a strong excess particularly between 20 and 40 keV and yields a poor fit ($\chi^2/\nu = 893.0/762$) as shown in Fig. 7. The harder shape of the spectrum in slice B due to a higher obscuration compared to slice A.

We then explored a more complex geometry of the reprocessor by adopting the 'decoupled' configuration of `MYTorus` defined as model $\mathcal{C}$. By following the methodology presented in details in Yaqoob (2012), we want to represent a physical scenario where the neutral absorber is inhomogeneous in nature and hence characterized by a more 'patchy' distribution of reprocessing clouds. This can be achieved by decoupling the inclination angle parameters of the zeroth-order (line-of-sight) and reflected continua and allowing the corresponding column density defined as $N_{\rm H,Z}$ (line-of-sight $N_{\rm H}$) and $N_{\rm H,S}$ (global $N_{\rm H}$), respectively. The inclination of the zeroth-order component is fixed at 90° whereas the re-

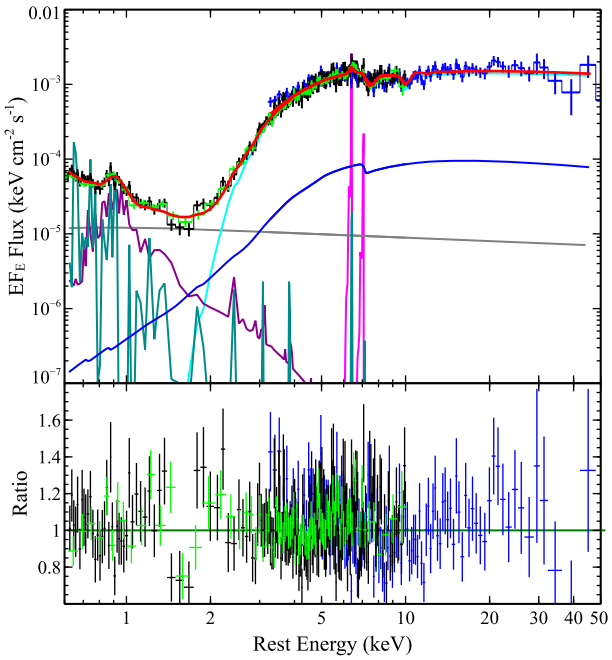

Figure 6. Top panel: The simultaneous *XMM–Newton* and *NuSTAR* data of MCG–03–58–007 corresponding to slice A. The fluxed spectra was unfolded against a simple power law with $\Gamma = 2$ with the best-fitting model $\mathcal{B}$ superimposed shown in red. The pn, MOS 1 + 2, and FPMA+B spectra are shown in black, green, and blue, respectively, where the latter have been only co-added for plotting purposes. The contribution of model $\mathcal{B}$ are distant scattered component (grey), photoionized emission (dark cyan), hot thermal emission (dark magenta), whereas the corresponding `MYTorus` model contributions are the (zeroth-order) transmitted absorbed primary component (cyan), the reflected component (blue), and the Fe Kα and Fe Kβ fluorescent line emission lines (magenta). Bottom panel: The corresponding data/model ratio which shows some residual left > 10 keV.

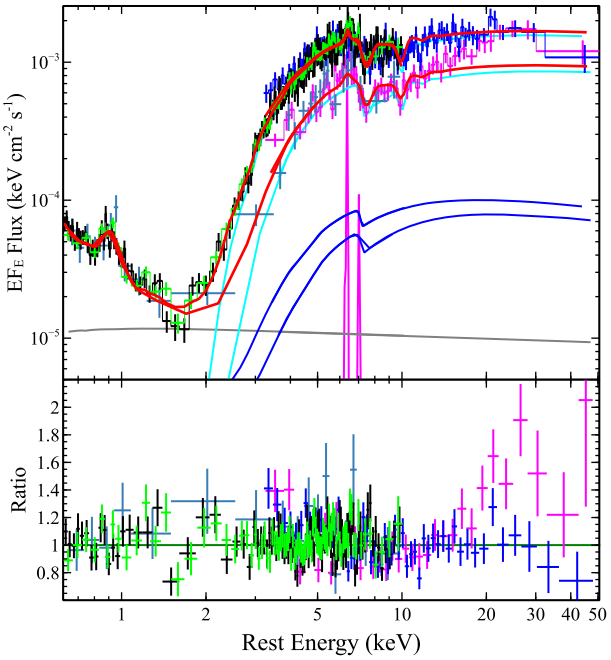

Figure 7. Top panel: Best-fitting model $\mathcal{B}$ superimposed (red) between slices A and B. The corresponding `MYTorus` model contributions are (zeroth-order) transmitted absorbed primary component (cyan), the reflected continuum (blue), and the Fe Kα and Fe Kβ fluorescent line emission lines (magenta). The distant scattered component is shown in grey. Bottom panel: The corresponding data/model ratio which show a clear excess in the residuals above 20 keV in slice B, which cannot be accounted for in the coupled `MYTorus` model. The separate thermal and photoionized components are not included in the plot for clarity (but are included in the model). Note that for plotting purposes we adopted the combined *NuSTAR* FPMA+FPMB spectra.

flected component at 0°. The fluorescence emission lines, and the relative normalizations are all tied to the primary power law i.e. $\mathrm{norm_{S00}} = \mathrm{norm_{L00}} = \mathrm{norm_{S90}} = \mathrm{norm_{intr\,zpowl}}$. As in model $\mathcal{B}$, all the corresponding constant factors $\mathrm{A_{S00}} = \mathrm{A_{L00}} = \mathrm{A_{S90}}$ are set to unity.

In this model, we find that the global $N_{\rm H}$ is much larger than the zeroth-order at $\log(N_{\rm H,S}/{\rm cm}^{-2}) = 24.7^{+0.4}_{-0.1}$ which imprints a much stronger reflection component in the spectrum. Although better than the coupled configuration, model $\mathcal{C}$ still forces a ∼40 per cent decrease of the primary continuum which still produces some excess residuals in slice B between 20 and 40 keV (see bottom-left panel in Fig. 8). Although the transmitted $N_{\rm H}$ increases and hence explain well the spectral curvature in slice B, is still not enough to fully account for it (see top-left panels in Fig. 8). Instead, this seems to suggest that an additional variable absorber, such as the wind, is required to explain the increase in hardness of slice B. In summary by investigating case (i) with model $\mathcal{C}$, resulted in an improved fit compared to model $\mathcal{B}$ at $\chi^2/\nu = 860.7/761$ (corresponding to a > 99.99 per cent improvement). Even if the fit statistically improves, model $\mathcal{C}$ is not able to fully reproduce the spectral shape of slice B, leaving strong residuals in the 20–40 keV range. Subsequently we tested case (ii) with model $\mathcal{C}$ by keeping the transmitted $N_{\rm H,Z}$ of the `MYTorus` model tied between slices, but allowing the column density of the slower ($v_{\rm w}/c = 0.1$) zone to vary. In Fig. 8 (right-hand panels), we show the best-fitting model $\mathcal{C}$ for case (ii) overlaid on the fluxed slice A and B spectra (top) and the corresponding residuals (bottom). This time the spectral curvature in slice B is well reproduced. This is explained by a drastic increase in column density of the slower ionized absorber (zone 1) by almost one order of magnitude i.e. from $\log(N_{\rm H}/{\rm cm}^{-2}) = 23.2 \pm 0.1$ to $\log(N_{\rm H}/{\rm cm}^{-2}) = 24.0 \pm 0.1$ between slice A and slice B.

In summary, the observed variability of spectral hardness and line-of-sight column density is best modelled by a change in $N_{\rm H}$ of the ionized absorber rather than by neutral absorption. Moreover, as in B18, we also found that there is no improvement in the fit by letting the $N_{\rm H}$ of the fast zone 2 to vary, hence suggesting that the density change in the $v_{\rm w}/c = 0.1$ zone is what drives the observed variability. We also found that the overall power-law normalization does not decrease as drastically (∼10 per cent) and the model now converges at ∼20 keV, hence all the variations occur at lower energies due to absorption variability. Thus, this model led to an excellent fit to the overall data at $\chi^2/\nu = 826.4/761$, providing a substantial improvement of $\Delta\chi^2/\Delta\nu = 34.3/1$ (i.e. $\sim 6\sigma$).

5 DISCUSSION AND CONCLUSION

We presented a detailed broad-band spectral analysis of the X-ray spectra emission within 0.6–50 keV of MCG–03–58–007, where we successfully de-convolved, by using `MYTorus`, all the layers of absorption. We infer a complex structure of absorbers consisting of (a) a primary power-law component absorbed by a fully covering neutral medium likely associated with the inhomogeneous toroidal absorber, which is thicker in the equatorial plane, (b) a reflected

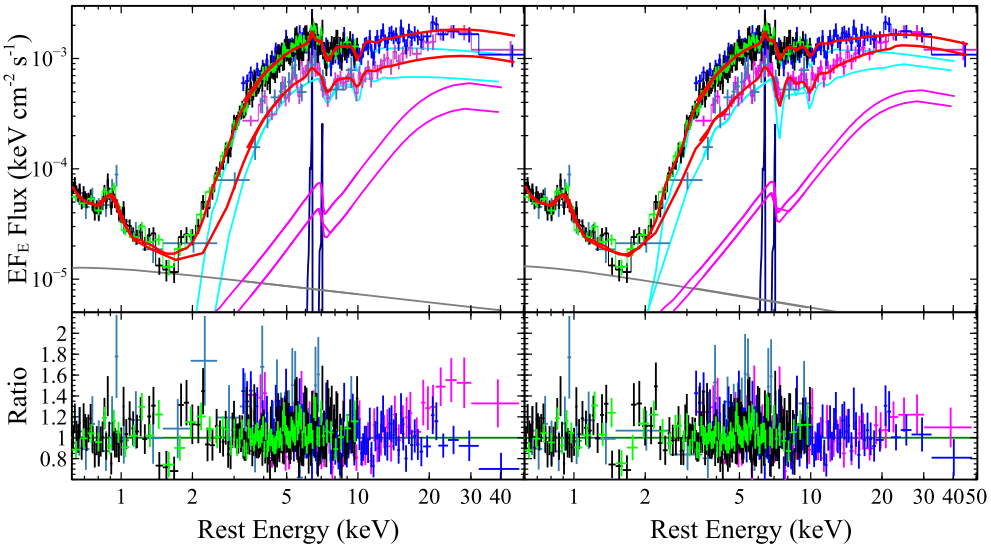

Figure 8. Best-fitting MYTorus decoupled mode (model *C*), applied to slice A and slice B where the left-hand panel shows a variable transmitted $N_{H,Z}$ (and constant wind), whereas the right-hand panel shows a constant transmitted $N_{H,Z}$ (and variable wind). Only the latter is able to fully account for the pronounced spectral curvature seen up to 40 keV in slice B. Note that for plotting purposes we adopted the combined *NuSTAR* FPMA+FPMB spectra. As the soft X-ray model components such as MEKAL and XSTAR emissions are not variable and do not affect the MYTorus parameters, we omitted them here for clarity. The distant scattered component is shown in grey and the MYTorus components are defined as in Fig. 7.

component from a distant reprocessor, and (c) a multiphase highly ionized fast outflow. In addition to this, we considered the analysis of the RGS data which allowed us to better understand the origin of the soft X-ray emission. Our main findings are summarized and discussed in the following.

5.1 The nature of the soft X-ray emission

The soft X-ray emission of MCG–03–58–007 can be well described with a superposition of a power-law scattered component and several narrow emission lines. The latter are associated with optically thin, photoionized gas as well as a weaker collisionally ionized plasma component consistent with starburst activities in the host galaxy. From the luminosity measured in the IR band, Oi, Imanishi & Imase (2010) were able to robustly estimate the star formation rate (SFR) in MCG–03–58–007 to be SFR $= 9.4\,M_{\odot}\,yr^{-1}$. From the SFR and the L_X–SFR correlations derived from various sample of LIRG and ULIRG (e.g. Ranalli, Comastri & Setti 2003; Pereira-Santaella et al. 2011; Mineo et al. 2014), we derived the predicted soft X-ray luminosity to be $L_{(0.5-2)\,keV} = 3 \times 10^{40}\,erg\,s^{-1}$ which is consistent with what it is measured in MCG–03–58–007 for the starburst component. In terms of the photoionized component, we measured a soft X-ray luminosity of $L_{(0.5-2)\,keV} \sim 10^{41}\,erg\,s^{-1}$.

We did not observe any variability in the soft band in respect to the 2010 *Suzaku* observation (see B18). All the emission lines are unresolved at the RGS spectral resolution ($\sigma_v \lesssim 1700\,km\,s^{-1}$). From the results outlined in Section 3.1, the O VII triplet ratio gave us an upper limit on the gas density of $n_e < 10^9\,cm^{-3}$ whereas from the photoionization modelling we obtained an ionization state of $\xi \sim 10\,erg\,cm\,s^{-1}$. Given the ionizing luminosity of $L_{ion} \sim 10^{45}\,erg\,s^{-1}$ in MCG–03–58–007, this places a lower limit on the radial distance of the gas of $R > 0.1$ pc. On the other hand, a subsequent *Chandra* imaging observation of MCG–03–58–007 in 2016 reveals that the soft X-ray emitter is largely point-like, within an arc second radius of the nucleus (Braito et al. in prep). For MCG–03–58–007 this corresponds to an emitting gas that is confined within a scale of few hundreds of parsec and although this distance scale is poorly constrained, it is likely constant with NLR gas on approximately parsec scales or greater as often seen in other Seyfert 2 galaxies (e.g. Sako et al. 2000; Kinkhabwala et al. 2002; Braito et al. 2017). As shown in Fig. 4, the dominant contributor to the emission lines is mostly a distant gas photoionized by the AGN often observed in Seyfert 2 galaxies (e.g. Guainazzi & Bianchi 2007). However, in all the adopted models we also observed a contribution from a weak thermal emission component with temperature of $kT \sim 0.8$ keV. Note that if we did not include the photoionized emission, the luminosity of the emission lines component (parametrized with MEKAL) would be simply too high with respect to the soft X-ray luminosity expected from the SFR.

5.2 X-ray broad-band variability: clumpy torus or highly ionized disc-wind

The variability in the *XMM–Newton* and *NuSTAR* spectra in MCG–03–58–007 was caused by a rapid eclipsing event as discussed in B18. In this work, we further investigated the cause of this event. We initially tested a scenario where the variability between the slices (defined in Section 4.1) could be explained solely with a change in N_H of the neutral absorber and the primary continuum normalization by adopting the coupled MYTorus configuration whilst keeping the disc-wind XSTAR parameters fixed between the slices. As discussed in Section 4.3, in the coupled MYTorus configuration the column densities of the transmitted and reflected components are coupled together (i.e. have the same N_H). We found that in this scenario the N_H only increased by ∼30 per cent, while the primary continuum decreased by ∼50 per cent. Moreover, as there is no spectral variability between the slices > 20 keV, the excessive drop in normalization fails to account for the sharp hardening in the spectrum in slice B. This results in a very prominent excess residuals in the *NuSTAR* spectrum above 20 keV in slice B as shown in Fig. 7.

In B18, it was tested whether the spectral variability could be explained by the presence of a classical clumpy neutral absorber. Al-

though it produced an acceptable fit, this scenario was also ruled out due to its excessively high column density at $\log(N_{\rm H}/{\rm cm}^{-2}) > 24.5$ which required ∼99 per cent covering (during slice B) and the unphysically high luminosity derived when Compton (down)scattering effects were taken to account for such high $N_{\rm H}$. In this work, we attempted to test the above scenario with the more physical MYTorus model by decoupling the $N_{\rm H}$ of the out of line-of-sight reflected and zeroth-order (transmitted) components (model *C*). The patchy distribution of the reprocessor assumed in model *C* allowed us to better account for the spectral curvature in slice B (see Section 4.2.1). Despite this, the overall normalization of the primary continuum still excessively decreased and hence significant residuals were still present $\gtrsim$20 keV in slice B (see left-hand panel of Fig. 8).

When fitting the *XMM–Newton* and *NuSTAR* data with the MYTorus decoupled mode, we were able to measure the column densities of both the out of the line-of-sight and transmitted reprocessors. Remarkably, we found that the measured global $N_{\rm H,S}$ was indeed much larger that the line-of-sight $N_{\rm H,Z}$ by at least an order of magnitude (see Table 4). Such an extreme difference between these two absorbers can be geometrically explained with an overall patchy toroidal reprocessor which is broadly Compton-thin with a relatively small equatorial thick layer out of the line of sight as shown schematically in Fig. 9.

MCG–03–58–007 is not an outlier in this respect, in fact the difference between the global and zeroth-order $N_{\rm H}$ which suggest an inhomogeneous torus has been already observed in other Seyfert 2 galaxies such as e.g. NGC 4945 (Yaqoob 2012), Markarian 3 (Yaqoob et al. 2015). This sort of inhomogeneous nature of the torus has been widely accepted in the scientific community by developing torus models considering a clumpy gas distribution (e.g. Elitzur & Shlosman 2006; Nenkova et al. 2008a,b). Furthermore in the most recent models, the overall absorption can be quantified more as a viewing probability dependent on the physical properties of the cloud i.e. size and location, which typically tend to be distributed towards the equatorial plane.

Our modelling with the self-consistent model for a toroidal absorber confirms that the main driver for the observed variability is the wind rather than a clumpy neutral absorber. In all the models tested, when the wind column is held constant between the slices, the models require the normalization of the primary continuum to drop in slice B to compensate, leaving an excess above 20 keV in the residuals. However, this can be ruled out, as such a drop in the continuum is not seen in the 20–40 keV light-curve. Instead, if the wind $N_{\rm H}$ is allowed to increase in slice B, then this can naturally account for the increase in hardness of slice B, while the overall continuum normalization is now constant, consistent with the lack of variability above 20 keV. Thus, this result suggested at high confidence level > 99.99 per cent that the eclipsing event was not caused by a neutral absorber in the clumpy torus but instead driven by a transiting clump (or filament) in an inhomogeneous and highly ionized disc-wind located a few hundreds of $R_{\rm g}$ from the black hole (B18). Indeed such rapid absorption event caused by the highly ionized disc-wind was also observed in PDS 456 (Gofford et al. 2014; Matzeu et al. 2016), which is considered to be hosting the prototype disc-wind (Reeves et al. 2018), as well as e.g. in PG 1211+143 (Pounds et al. 2003), PG 1126–041 (Giustini et al. 2011) and APM 08279+5255 (Chartas et al. 2003). Despite the lower X-ray luminosity that characterizes MCG–03–58–007, the presence of such powerful and highly variable disc-wind resembles the one observed in the more powerful quasars with the addition that they are not usually observed in standard obscured Seyfert galaxies. The presence of variable ionized inhomogeneous outflows have also been observed in the UV band, located at larger distance ∼0.01–10 pc (e.g. Capellupo et al. 2013; McGraw et al. 2018), which are increasingly supporting the multiphase structure of these winds. For example, in the narrow-line Seyfert 1 galaxy WPVS 007, Leighly et al. (2015) observed for the first time an occultation event in the UV associated with broad absorption line gas in the torus; whereas in the Seyfert 1 galaxy NGC 5548 an ongoing long-term obscuration is observed in both the X-rays and UV bands (Kaastra et al. 2014). Interestingly, Hamann et al. (2018) detected a fast UV counterpart of the X-ray wind in PDS 456 which was measured at a comparable outflow velocity of $v_{\rm w} \sim 0.3c$.

5.3 Physical properties and location of the clumpy disc-wind

Now we investigate the main properties of the highly ionized fast disc-wind and compare them with the results obtained in B18. From the observed outflow velocity ($v_{\rm w}$) inferred from the two blueshifted Fe K absorption features, we can estimate a lower limit on the launching radius. This can be done by equating the $v_{\rm w}$ with its escape radius, thus $R_{\rm esc} = (2c^2/v_{\rm w}^2)R_{\rm g}$ where $R_{\rm g} = GM_{\rm BH}/c^2$ is the gravitational radius which corresponds to $1R_{\rm g} \sim 1.5 \times 10^{13}$ cm for a black hole mass of $M_{\rm BH} \sim 10^8\,{\rm M}_{\odot}$ in MCG–03–58–007 (B18). We therefore derive $R_{\rm in,1} \sim 140\,R_{\rm g}$ ($\sim 2 \times 10^{15}$ cm) and $R_{\rm in,2} \sim 15\,R_{\rm g}$ ($\sim 2 \times 10^{14}$ cm) for zone 1 ($v_{\rm w}/c = -0.12^{+0.02}_{-0.01}$) and zone 2 ($v_{\rm w}/c = -0.36 \pm 0.02$), respectively. These results suggest that we are viewing the disc-wind through a line of sight that intercepts two distinct streamlines launched at different radii as also observed in PDS 456 (Reeves et al. 2018). We then utilize these measurements to estimate the disc-wind energetics by quantifying the mass outflow rate ($\dot{M}_{\rm w}$) expressed as $\dot{M}_{\rm w} = f\mu\pi m_{\rm p} v_{\rm w} N_{\rm H} {\rm R}_{\rm in}$, derived by Krongold et al. (2007), where a biconical geometry of the outflow is assumed. The constant factor for cosmic elemental abundances is set to $\mu = n_{\rm H}/n_{\rm e} = 1.2$ and $R_{\rm in}$ is the inner radius or the starting point of the disc-wind. The function f takes into account the inclination angle with respect to the line of sight and the disc. Unlike in PDS 456, where the disc-wind's solid angle was directly measured (Nardini et al. 2015), the geometry of the system in MCG–03–58–007 is currently uncertain and hence we adopt a face value of $f = 1.5$ (see appendix 2 in Krongold et al. 2007).

Thus, for the slow zone 1, observed in slice A, we obtain a mass outflow rate of $\dot{M}_{\rm w,z1} \sim 1.2 \times 10^{25}\,{\rm g\,s^{-1}}$ ($\sim 0.3\,{\rm M}_{\odot}\,{\rm yr}^{-1}$) which implies a kinetic power of $\dot{E}_{\rm w,z1} \sim 8 \times 10^{43}\,{\rm erg\,s^{-1}}$. This corresponds to ∼3 per cent of the bolometric luminosity and hence falls within the, theoretically predicted, minimum requirement i.e. $\dot{E}_{\rm w}/L_{\rm bol} \sim 0.5$–5 per cent for providing a feedback mechanisms between the central SMBH and its host galaxy (e.g. Di Matteo et al. 2005; Hopkins & Elvis 2010). This result is consistent with B18 with the only difference being that a constant $v_{\rm w}$ is assumed across the modelling. On the other hand, in slice B, the drastic increase in $N_{\rm H}$ results in a considerably higher kinetic power of $\dot{E}_{\rm w,z1} \sim 5 \times 10^{44}\,{\rm erg\,s^{-1}}$ which corresponds to ∼15 per cent of $L_{\rm bol}$ and hence exceeding the typical values quoted by AGN feedback models. By assuming that the outflow velocity is comparable to the Keplerian velocity across the source i.e. $v_{\rm K} \sim v_{\rm w} = 0.12c$ and from the measured timescale of this obscuration event $\Delta t = 120$ ks we derive the radial size of the absorber to be $\Delta R_{\rm c} = v_{\rm K}\Delta t \sim 30 R_{\rm g}$ ($\sim 4 \times 10^{14}$ cm). The hydrogen number density of the cloud is defined as

$$n_{\rm H} \sim \frac{\Delta N_{\rm H}}{\Delta R_{\rm c}} \sim \frac{\Delta N_{\rm H} r_{\rm g}^{1/2}}{\sqrt{2} c \Delta t}, \qquad (2)$$

Table 4. Summary of the broad-band best-fitting parameters of model $\mathcal{C}$ applied for slice A and slice B of *XMM–Newton* and *NuSTAR* (see the text for details). The important outcome of this result is that the observed spectral variability between the slices can be explained by a drastic increase in $N_{\rm H}$ by a factor of $\sim$10 $\times$ in zone 1 of the highly ionized absorber as opposed to a change in the $N_{\rm H}$ of the neutral absorber. This behaviour suggests at a high confidence level (>99.99%) that the observed spectral variability is caused by the highly ionized material rather than a neutral inhomogeneous absorber. All the parameters and units are the same as in Table 3.

Component	Parameter	Model $\mathcal{C}$ (decoupled, wind fix)		Model $\mathcal{C}$ (decoupled, wind vary)	
		Continuum			
		Slice A	Slice B	Slice A	Slice B
Primary power-law	Γ	$2.29^{+0.05}_{-0.07}$	$2.29^{\rm t}$	$2.36^{+0.06}_{-0.06}$	$2.36^{\rm t}$
	norm[a]	$3.6^{+0.5}_{-0.5}$	$2.3^{+0.4}_{-0.5}$	$4.2^{+0.5}_{-0.4}$	$3.5^{+0.8}_{-0.6}$
Scattered continuum	Γ	$2.29^{\rm t}$	$2.29^{\rm t}$	$2.36^{\rm t}$	$2.36^{\rm t}$
	norm[b]	$1.4^{+0.2}_{-0.2}$	$1.4^{\rm t}$	$1.3^{+0.2}_{-0.2}$	$1.3^{\rm t}$
		Soft X-ray emission			
Photoionized emission	$\kappa_{\rm xstar}$ ($\times 10^{-6}$)	$1.8^{+0.2}_{-0.2}$	$1.8^{\rm t}$	$1.7^{+0.2}_{-0.2}$	$1.7^{\rm t}$
Thermal emission	kT (keV)	$0.78^{+0.05}_{-0.05}$	$0.78^{\rm t}$	$0.78^{+0.05}_{-0.05}$	$0.78^{\rm t}$
	norm ($\times 10^{-5}$)	$1.5^{+0.2}_{-0.2}$	$1.5^{\rm t}$	$1.5^{+0.2}_{-0.2}$	$1.5^{\rm t}$
		Distant reprocessor and neutral absorber			
MYTorus	Γ	$2.29^{\rm t}$	$2.29^{\rm t}$	$2.36^{\rm t}$	$2.36^{\rm t}$
	$\log(N_{\rm H,S}/{\rm cm}^{-2})$	$24.7^{+0.4}_{-0.1}$	$24.7^{\rm t}$	>24.6	>24.6[t]
	$\log(N_{\rm H,Z}/{\rm cm}^{-2})$	$23.16^{+0.03}_{-0.02}$	$23.34^{+0.05}_{-0.05}$	$23.16^{+0.02}_{-0.02}$	$23.16^{\rm t}$
	$\rm norm_{S00} = norm_{L00} = norm_{S90}$	$3.6^{\rm t}$	$2.3^{\rm t}$	$4.2^{\rm t}$	$3.5^{\rm t}$
		Highly ionized absorber			
Zone 1	$\log(N_{\rm H}/{\rm cm}^{-2})$	$23.1^{+0.1}_{-0.1}$	$23.1^{\rm t}$	$\mathbf{23.2}^{+0.1}_{-0.1}$	$\mathbf{24.0}^{+0.1}_{-0.1}$
	$\log(\xi/{\rm erg\,cm\,s}^{-1})$	$4.3^{+0.1}_{-0.1}$	$4.3^{\rm t}$	$4.1^{+0.1}_{-0.1}$	$4.1^{\rm t}$
	$v_{\rm w}/c$	$-0.11^{+0.01}_{-0.02}$	$-0.11^{\rm t}$	$-0.12^{+0.02}_{-0.01}$	$-0.12^{\rm t}$
Zone 2	$\log(N_{\rm H}/{\rm cm}^{-2})$	$24.0^{+0.1}_{-0.1}$	$24.0^{\rm t}$	$23.9^{+0.2}_{-0.3}$	$23.9^{\rm t}$
	$\log(\xi/{\rm erg\,cm\,s}^{-1})$	$6.2^{+0.4}_{-0.9}$	$6.2^{\rm t}$	$6.2^{+0.5}_{-0.9}$	$6.2^{\rm t}$
	$v_{\rm w}/c$	$-0.36^{+0.02}_{-0.02}$	$-0.36^{\rm t}$	$-0.36^{+0.02}_{-0.02}$	$-0.36^{\rm t}$
Cross-normalization	MOS	0.95 ± 0.02	–	0.95 ± 0.02	–
	FPMA	1.05 ± 0.04	$0.98^{+0.11}_{-0.09}$	1.07 ± 0.04	$0.98^{+0.10}_{-0.09}$
	FPMB	$1.11^{+0.04}_{-0.05}$	$1.00^{+0.12}_{-0.10}$	1.12 ± 0.04	$1.00^{+0.10}_{-0.09}$
Fit statistic	χ^2/ν	860.7/761		826.4/761	

where $\Delta N_{\rm H}$ is the observed change in column density between slice A and slice B and $r_{\rm g} = R/R_{\rm g}$ is the radial distance in units of $R_{\rm g}$. From the definition of the ionization parameter i.e. $L_{\rm ion}/n_{\rm H}R^2$ (Tarter, Tucker & Salpeter 1969), we have $n_{\rm H} \sim n_{\rm e} = L_{\rm ion}/\xi R^2$ and hence equating these densities we get

$$r_{\rm g}^{5/2} = \frac{L_{\rm ion}}{\xi} \frac{\sqrt{2}\Delta t\, c^5}{\Delta N_{\rm H}} (G M_{\rm BH})^{-2}\,. \quad (3)$$

From an ionization of $\xi \sim 13\,000$ erg cm s^{-1}, an observed change in column density of $\Delta N_{\rm H} \sim 8.4 \times 10^{23}$ cm^{-2} (obtained in model $\mathcal{C}$) and by assuming an ionizing luminosity of the order of $L_{\rm ion} \sim 10^{45}$ erg s^{-1}, the location of the eclipsing cloud is derived to be $R \sim 340\ R_{\rm g}$ (5×10^{15} cm), which is consistent to what was measured in B18. These results suggest that we are viewing through a clumpy disc-wind at a typical distance of few hundreds of $R_{\rm g}$ from the central black hole, launched between tens to hundreds of $R_{\rm g}$. Regarding the fast zone 2, the energetic that can be derived are purely speculative as, already noted in B18, the $N_{\rm H}$ can only be constrained by a given best-fitting ionization value as is otherwise degenerate with the ionization (see Section 4.2).

A physical picture of the possible geometry of such a system is schematically illustrated in Fig. 9 where the estimated distances of the launching radii of both zones and location of the eclipsing clump and distant circumnuclear gas are illustrated. From the overall information that it is gathered in this work, we have a scenario in which there are three main regions i.e. the highly ionized inhomogeneous fast outflows, the clumpy toroidal neutral absorbers, and the diffuse circumnuclear NLR scale gas. The highly ionized outflow is likely inhomogeneous in structure and it is located closer in to the SMBH, where the regions from high to lower ionization are shown in red to cyan, respectively. The clumpy torus is located at intermediate scales where we were able to measure two distinct column densities (in model $\mathcal{C}$) of the embedded neutral material (light to dark blue represent the increasing in $N_{\rm H}$).

The global $N_{\rm H,S}$ can be associated with a compact region of Compton-thick material that might be distributed equatorially out of our line of sight. On the other hand, the measured column density that intercept the line of sight ($N_{\rm H,Z}$) might be associated with Compton-thin material that is located at the edge of the clumpy torus. The diffuse circumnuclear gas is situated at larger scales (> BLR) where the photoionized and thermal emitters are illustrated in blue and green, respectively. The low covering factor that characterizes this gas might suggest that it is also inhomogeneous in structure where the dominant component can be associated

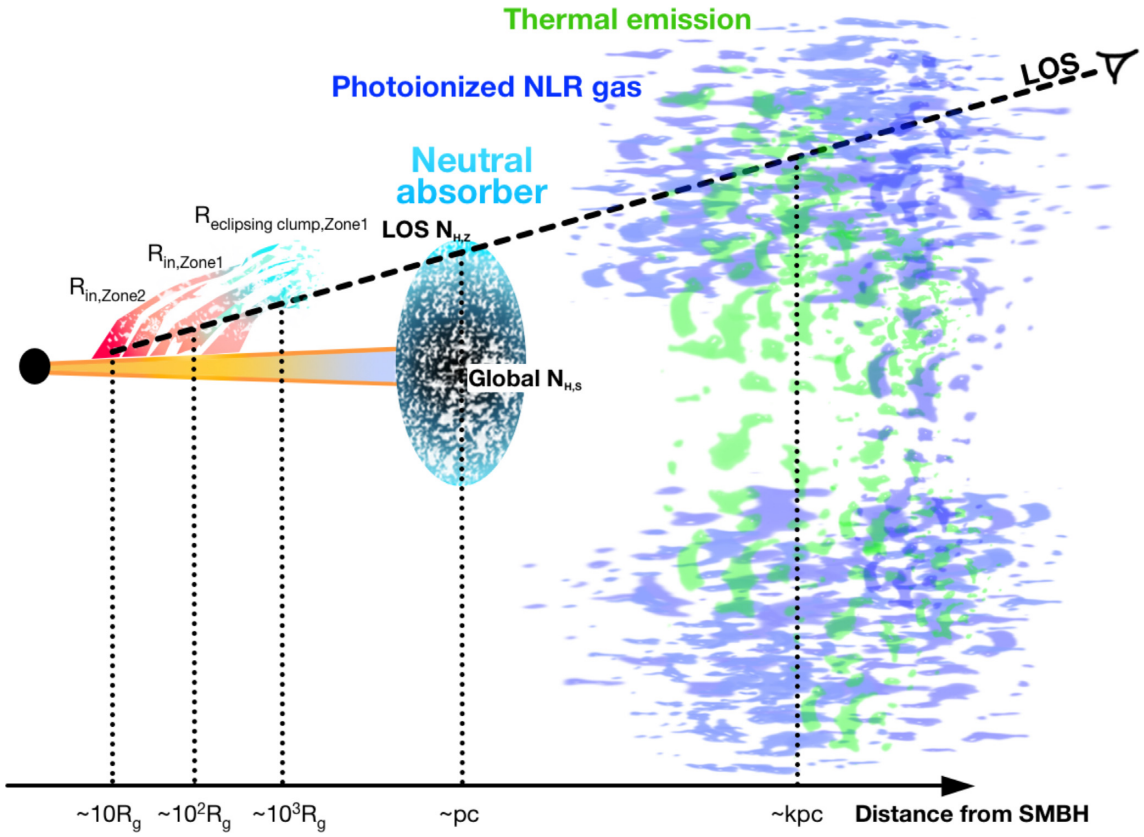

Figure 9. Schematic representation of the possible geometry for MCG–03–58–007. Our line of sight is represented by the dashed line. The different components of the system are shown with the corresponding distance scales from the SMBH. Here there are three main regions i.e. the highly ionized outflow, the clumpy torus, and the diffuse NLR gas are illustrated. The highly ionized outflow is located closer in, where the regions from high to lower ionization are shown in red to cyan, respectively. The launch radii and location of the eclipsing ionized cloud of outflowing material are reported. The clumpy torus is located at intermediate scales where the two distinct column densities (measured in the `MYTorus` decoupled mode) of the embedded neutral material are indicated. The global $N_{H,S}$ is possibly associated with Compton-thick material might be distributed equatorially. On the other hand, the measured column density that crosses the line of sight ($N_{H,Z}$) is associated with Compton-thin material that may be located at the edge of the clumpy torus. The diffuse gas is located at larger scales where the photoionized and thermal emitters are illustrated in blue and green, respectively.

with photoionized emission caused by the AGN. Although MCG–03–58–007 is classified as Seyfert 2 galaxy the fortuitous line of sight (black dash line) through Compton-thin material. Thanks to the synergy between *XMM–Newton* and *NuSTAR* X-ray observatories, it was possible to build a complete picture of this complex system.

ACKNOWLEDGEMENTS

We want to thank the referee for the detailed and helpful report that improved the clarity of this paper. GAM also thanks Dr Emanuele Nardini for the useful discussions. GAM and MLP are supported by European Space Agency (ESA) Research Fellowships. Based on observations obtained with *XMM–Newton*, an ESA science mission with instruments and contributions directly funded by ESA Member States and NASA. GAM, VB, PS, AC, and RDC acknowledge support from the Italian Space Agency (contracts ASI-INAF I/037/12/0 and ASI-INAF 2017-14-H.0). JNR acknowledges financial support through grants NNX17AC38G, NNX17AD56G, and *HST*-GO-14477.001-A. CC acknowledges funding from the European Union's Horizon 2020 research and innovation programme under the Marie Skłodowska-Curie grant agreement no. 664931.

REFERENCES

Antonucci R., 1993, ARA&A, 31, 473
Arnaud K. A., 1996, in Jacoby G. H., Barnes J., eds, ASP Conf. Ser. Vol. 101, Astronomical Data Analysis Software and Systems V. Astron. Soc. Pac., San Francisco, p. 17
Bautista M. A., Kallman T. R., 2001, ApJS, 134, 139
Blustin A. J., Page M. J., Fuerst S. V., Branduardi-Raymont G., Ashton C. E., 2005, A&A, 431, 111
Braito V., Reeves J. N., Bianchi S., Nardini E., Piconcelli E., 2017, A&A, 600, A135
Braito V. et al., 2018, MNRAS, 479, 3592
Capellupo D. M., Hamann F., Shields J. C., Halpern J. P., Barlow T. A., 2013, MNRAS, 429, 1872
Cash W., 1979, ApJ, 228, 939
Chartas G., Brandt W. N., Gallagher S. C., Garmire G. P., 2002, ApJ, 579, 169
Chartas G., Brandt W. N., Gallagher S. C., 2003, ApJ, 595, 85
Cicone C. et al., 2014, A&A, 562, A21
Cicone C. et al., 2018, ApJ, 863, 143
Dickey J. M., Lockman F. J., 1990, ARA&A, 28, 215
Di Matteo T., Springel V., Hernquist L., 2005, Nature, 433, 604
Elitzur M., Shlosman I., 2006, ApJ, 648, L101
Feruglio C. et al., 2015, A&A, 583, A99
Giustini M. et al., 2011, A&A, 536, A49

Gofford J., Reeves J. N., Tombesi F., Braito V., Turner T. J., Miller L., Cappi M., 2013, MNRAS, 430, 60
Gofford J. et al., 2014, ApJ, 784, 77
Guainazzi M., Bianchi S., 2007, MNRAS, 374, 1290
Hamann F., Chartas G., Reeves J., Nardini E., 2018, MNRAS, 476, 943
Hopkins P. F., Elvis M., 2010, MNRAS, 401, 7
Kaastra J. S., Mewe R., Liedahl D. A., Komossa S., Brinkman A. C., 2000, A&A, 354, L83
Kaastra J. S. et al., 2014, Science, 345, 64
Kallman T. R., Palmeri P., Bautista M. A., Mendoza C., Krolik J. H., 2004, ApJS, 155, 675
Kallman T., Evans D. A., Marshall H., Canizares C., Longinotti A., Nowak M., Schulz N., 2014, ApJ, 780, 121
King A., 2003, ApJ, 596, L27
King A. R., Pounds K. A., 2003, MNRAS, 345, 657
Kinkhabwala A. et al., 2002, ApJ, 575, 732
Krongold Y., Nicastro F., Elvis M., Brickhouse N., Binette L., Mathur S., Jiménez-Bailón E., 2007, ApJ, 659, 1022
Leighly K. M., Cooper E., Grupe D., Terndrup D. M., Komossa S., 2015, ApJ, 809, L13
Markowitz A. G., Krumpe M., Nikutta R., 2014, MNRAS, 439, 1403
Matzeu G. A., Reeves J. N., Nardini E., Braito V., Costa M. T., Tombesi F., Gofford J., 2016, MNRAS, 458, 1311
Matzeu G. A., Reeves J. N., Braito V., Nardini E., McLaughlin D. E., Lobban A. P., Tombesi F., Costa M. T., 2017, MNRAS, 472, L15
McGraw S. M., Shields J. C., Hamann F. W., Capellupo D. M., Herbst H., 2018, MNRAS, 475, 585
Mewe R., Gronenschild E. H. B. M., van den Oord G. H. J., 1985, A&AS, 62, 197
Mineo S., Gilfanov M., Lehmer B. D., Morrison G. E., Sunyaev R., 2014, MNRAS, 437, 1698
Murphy K. D., Yaqoob T., 2009, MNRAS, 397, 1549
Nandra K., O'Neill P. M., George I. M., Reeves J. N., 2007, MNRAS, 382, 194
Nardini E., Fabian A. C., Reis R. C., Walton D. J., 2011, MNRAS, 410, 1251
Nardini E. et al., 2015, Science, 347, 860
Nenkova M., Sirocky M. M., Ivezić Ž., Elitzur M., 2008a, ApJ, 685, 147
Nenkova M., Sirocky M. M., Nikutta R., Ivezić Ž., Elitzur M., 2008b, ApJ, 685, 160
Netzer H., Laor A., 1993, ApJ, 404, L51
Oi N., Imanishi M., Imase K., 2010, PASJ, 62, 1509
Parker M. L. et al., 2017, Nature, 543, 83
Parker M. L., Matzeu G. A., Guainazzi M., Kalfountzou E., Miniutti G., Santos-Lleó M., Schartel N., 2018, MNRAS, 480, 2365
Pereira-Santaella M. et al., 2011, A&A, 535, A93
Pinto C. et al., 2018, MNRAS, 476, 1021
Porquet D., Dubau J., 2000, A&AS, 143, 495
Pounds K. A., Reeves J. N., King A. R., Page K. L., O'Brien P. T., Turner M. J. L., 2003, MNRAS, 345, 705
Ranalli P., Comastri A., Setti G., 2003, A&A, 399, 39
Reeves J. N., O'Brien P. T., Ward M. J., 2003, ApJ, 593, L65
Reeves J. N. et al., 2009, ApJ, 701, 493
Reeves J. N., Porquet D., Braito V., Gofford J., Nardini E., Turner T. J., Crenshaw D. M., Kraemer S. B., 2013, ApJ, 776, 99
Reeves J. N., Braito V., Nardini E., Lobban A. P., Matzeu G. A., Costa M. T., 2018, ApJ, 854, L8
Risaliti G., Elvis M., Nicastro F., 2002, ApJ, 571, 234
Sako M., Kahn S. M., Paerels F., Liedahl D. A., 2000, ApJ, 543, L115
Severgnini P., Caccianiga A., Della Ceca R., 2012, A&A, 542, A46
Singh K. P., Garmire G. P., Nousek J., 1985, ApJ, 297, 633
Tarter C. B., Tucker W. H., Salpeter E. E., 1969, ApJ, 156, 943
Tombesi F., Cappi M., Reeves J. N., Palumbo G. G. C., Yaqoob T., Braito V., Dadina M., 2010, A&A, 521, A57
Tombesi F., Meléndez M., Veilleux S., Reeves J. N., González-Alfonso E., Reynolds C. S., 2015, Nature, 519, 436
Turner T. J., Pounds K. A., 1988, MNRAS, 232, 463
Wilms J., Allen A., McCray R., 2000, ApJ, 542, 914
Yaqoob T., 2012, MNRAS, 423, 3360
Yaqoob T., Tatum M. M., Scholtes A., Gottlieb A., Turner T. J., 2015, MNRAS, 454, 973

This paper has been typeset from a TEX/LATEX file prepared by the author.